ARTICLE

https://doi.org/10.1038/s41467-021-24740-2 OPEN

Heterogeneous integration of single-crystalline rutile nanomembranes with steep phase transition on silicon substrates

Dong Kyu Lee[1,4], Yunkyu Park[1,4], Hyeji Sim[1,4], Jinheon Park[1], Younghak Kim[2], Gi-Yeop Kim[1], Chang-Beom Eom[3], Si-Young Choi[1]✉ & Junwoo Son[1]✉

Unrestricted integration of single-crystal oxide films on arbitrary substrates has been of great interest to exploit emerging phenomena from transition metal oxides for practical applications. Here, we demonstrate the release and transfer of a freestanding single-crystalline rutile oxide nanomembranes to serve as an epitaxial template for heterogeneous integration of correlated oxides on dissimilar substrates. By selective oxidation and dissolution of sacrificial VO_2 buffer layers from $TiO_2/VO_2/TiO_2$ by H_2O_2, millimeter-size TiO_2 single-crystalline layers are integrated on silicon without any deterioration. After subsequent VO_2 epitaxial growth on the transferred TiO_2 nanomembranes, we create artificial single-crystalline oxide/Si heterostructures with excellent sharpness of metal-insulator transition ($\Delta\rho/\rho > 10^3$) even in ultrathin (<10 nm) VO_2 films that are not achievable via direct growth on Si. This discovery offers a synthetic strategy to release the new single-crystalline oxide nanomembranes and an integration scheme to exploit emergent functionality from epitaxial oxide heterostructures in mature silicon devices.

[1] Department of Materials Science and Engineering, Pohang University of Science and Technology (POSTECH), Pohang, Republic of Korea. [2] Pohang Accelerator Laboratory, Pohang, Republic of Korea. [3] Department of Materials Science and Engineering, University of Wisconsin-Madison, Madison, WI, USA. [4]These authors contributed equally: Dong Kyu Lee, Yunkyu Park, Hyeji Sim. ✉email: youngchoi@postech.ac.kr; jwson@postech.ac.kr

Heteroepitaxial growth has been widely used to obtain single-crystal films for developing modern solid-state electronic and photonic devices[1,2]. In particular, epitaxial oxide heterostructures provide promise for emerging electronics and photonics due to the intriguing phenomena (e.g., metal-insulator transition (MIT)[3–6], high-electron mobility[7], ferroelectricity[8]) exhibited by these ionic crystals. Therefore, the stacking of single-crystalline oxide films on dissimilar substrates (e.g., silicon (Si)) will offer ways to integrate the emergent phenomena of oxides with mature electronic and photonic devices[9–13]. However, the heteroepitaxial growth of oxide films drastically limits the possible material combinations due to the requirement of lattice matching between the epilayer and substrate[14]. For instance, direct oxide growth on dissimilar materials typically forms defective or polycrystalline layers near the interface between films and substrates[15,16], preventing unrestricted integration of single-crystal oxide films onto any desired substrates, especially on mainstream Si substrates.

Release and transfer of freestanding single-crystal sheets with a nanoscale thickness (i.e., epitaxial lift-off for nanomembrane (NM)) gives the freedom to transfer the released epilayer onto highly mismatched or amorphous substrates, and even allows reusable substrates[9,17–21]. While crystalline materials that are intrinsically layered (e.g. two-dimensional (2D) materials) are exfoliated spontaneously due to weak van der Waals bonding between layers[22], the freestanding NM from three-dimensional (3D) oxide crystals with strong bonding is hindered by the technical challenges of lifting strongly bonded epitaxial films from the oxide substrates. Thus, the technique for releasing the freestanding NM from a host substrate essentially requires the preferential creation of bond breaking from the substrate.

Many techniques have been employed to form freestanding NMs with a mechanically cleavable plane. For example, physical release methods (e.g., laser lift-off[20]) were originally developed to release epitaxial GaN semiconductor films to break strong bonding. However, these methods are only applicable to the formation of thick semiconductor membranes due to the inevitable structural damage. Moreover, a few monolayers of graphene could be inserted to release single-crystalline oxide membranes from substrates (i.e., “remote” epitaxy). Despite the versatility of this technique, the coalescence of localized nuclei in oxide layers on the graphene, along with the restriction of oxygen environment during growth, prevents the layer-by-layer growth of ultrathin oxide NM with atomic precision and high quality[10].

By contrast, the freestanding NM was chemically released from the substrate by selective etching of sacrificial layers[18,19,21]; these chemical lift-off methods are less destructive than physical methods. However, the harsh wet condition with a strong acid or base etchant typically leaves roughening and residue on the host substrates or released membrane after the chemical etch[23,24]. Recently, atomically thin perovskite oxide NM was gently released by dissolving water-soluble $Sr_3Al_2O_6$ sacrificial layers[11], but the moisture-sensitive nature of these layers prevents long-time exposure of the sacrificial layers, which restricts practical application for heterogeneous integration of oxide NM. Moreover, the development of oxide NM has been limited for perovskite structure among chemical lift-off methods so far[10–12,21,25,26]; to extend the materials spectrum for freestanding oxide NM, a new combination of the sacrificial layer and etchant needs to be developed for the heterogeneous integration of epitaxial oxide NM with other crystal structures on dissimilar substrates[10].

Here, we demonstrate that single-crystalline rutile oxide NM with the sharpened MIT can be integrated on the technologically influential, but more challenging, Si substrates by new epitaxial lift-off combination (see Fig. 1 for the process schematic). After the synthesis of an epitaxial TiO_2/VO_2 heterostructure on TiO_2 host substrate (Fig. 1a), the VO_2 sacrificial layer is selectively dissolved in dilute H_2O_2 to release the top TiO_2 film with the mechanical supporting layers (Fig. 1b). Contrary to the previous chemical lift-off using extreme pH solution, dilute aqueous H_2O_2 with mild pH leads to selective etching of epitaxially grown VO_2 sacrificial films by phase transformation to two-dimensional layered structure with weak bonding; this selective dissolution of VO_2 layer releases millimeter-scale freestanding TiO_2 NM from the $TiO_2/VO_2/TiO_2$ heterostructures at room temperature. Then, the single-crystalline TiO_2 NM is transferred onto the Si substrates without any deterioration of crystal quality (Fig. 1c, d). Interestingly, transferred TiO_2 single-crystal NM serves as a template for the heterogeneous integration of single-crystal VO_2 films on Si substrate (Fig. 1e). As a result of the VO_2 film epitaxially grown on TiO_2 NM template, more than three orders of

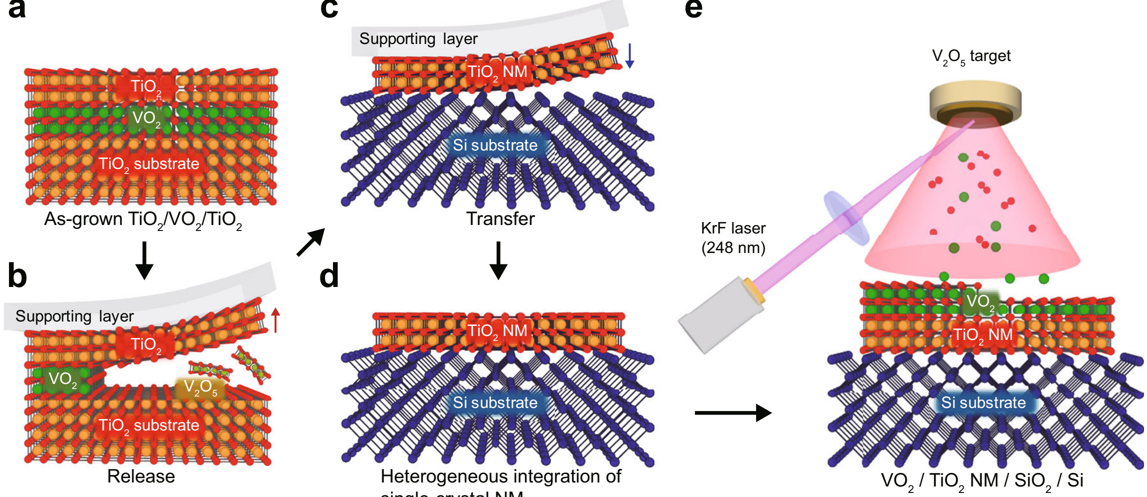

Fig. 1 Process schematic for single-crystal rutile oxide nanomembranes (NM) on silicon. **a** Schematic of an epitaxial TiO_2/VO_2 heterostructure on TiO_2 host substrate. **b** The VO_2 layer is dissolved in H_2O_2 to release the top TiO_2 film with the mechanical supporting layer. **c** The freestanding TiO_2 NM is transferred onto the desired substrates (e.g., silicon). **d** By removing the rigid supporting layer, single-crystalline rutile oxide NM is heterogeneously integrated into a silicon substrate. **e** Epitaxial VO_2 film with steep phase transition is grown on the TiO_2-NM-templated Si substrates.

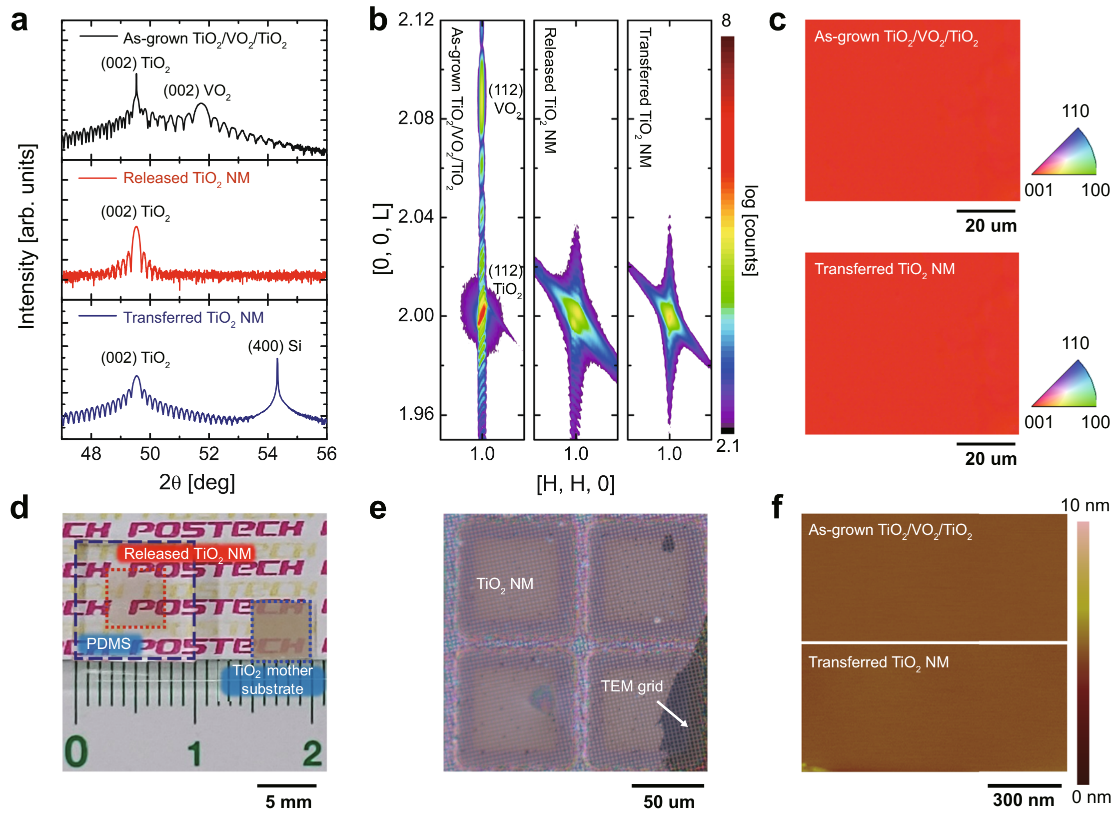

Fig. 2 Crystal and surface quality of released and transferred TiO_2 single-crystal nanomembrane (NM). a Symmetric $2\theta - \omega$ scan. **b** Reciprocal space mapping around (112) reflection of as-grown TiO_2 epitaxial films and TiO_2 single-crystal NM released on supporting layer and transferred on Si substrates. The high-resolution X-ray diffraction measurements show single-crystallinity with uniform out-of-plane orientation and no in-plane rotation in released and transferred TiO_2 NM. **c** EBSD maps of the as-grown TiO_2 epitaxial films on VO_2/TiO_2 substrates (top) and transferred TiO_2 NM on Si substrates (bottom), confirming the single-crystalline out-of-plane orientation. **d** Photograph of 40-nm-thick TiO_2 single-crystal NM released on mechanical support with the identical lateral dimension with TiO_2 host substrates. **e** OM image of transferred TiO_2 NM on the carbon TEM grid. **f** AFM image of as-grown TiO_2 films and transferred TiO_2 NM, which confirms a uniform and flat surface without surface cracks or residues.

magnitude modulation of resistivity ratio ($\Delta\rho/\rho > 10^3$) and sharpened MIT (i.e., narrow FWHM of Gaussian fitting from d $(\log_{10}(\rho))/\mathrm{d}T$ during heating and cooling (ΔT_h and ΔT_c ~3 K)) are remarkably achieved even in the ultrathin (≤10 nm) VO_2 films on Si substrates, which is not possible using conventional thin film growth.

Results

Synthesis of freestanding single-crystalline TiO_2 nanomembranes. Prior to release and transfer of TiO_2 NM, TiO_2 (10–70 nm)/VO_2 (~17 nm) heterostructures were epitaxially grown on (001)-oriented TiO_2 substrates by pulsed laser deposition (PLD) (Fig. 1a). Symmetrical 2θ-ω scan using synchrotron x-ray scattering on $TiO_2/VO_2/TiO_2$ detected two $(002)_R$ Bragg reflections, one from the rutile TiO_2 (2θ = 49.54°) film and substrate, and one from VO_2 film (2θ = 51.75°) (black line in Fig. 2a)[27]. Due to the close resemblance in crystal structure and small in-plane lattice mismatch of $(001)_R$-VO_2 and (001)-TiO_2 ($f_a \approx$ 0.86% along a- and b-axis), 17-nm-thick $(001)_R$-VO_2 films are fully strained by biaxial tensile strain; all heterostructure maintained identical in-plane lattice constant (left figure of Fig. 2b). Thus, the thickness of VO_2 (~17 nm) was determined to create unstrained and defect-free TiO_2 epitaxial films regardless of film thickness[27,28].

Then, rigid support layer (e.g., PDMS) was coated on the heterostructure before release to mechanically stabilize the TiO_2 NM and to facilitate the subsequent transfer of the released NM[10–12,25]. By simply immersing these $TiO_2/VO_2/TiO_2$ heterostructures into the dilute (10%) hydrogen peroxide (H_2O_2) solution at room temperature (Fig. 1b), a few millimeter-scale TiO_2 films were successfully released from their substrates by fully dissolving VO_2 sacrificial layers (i.e., denoted as released TiO_2 NM), allowing the growth substrate to be removed. The released single-crystal NM was transferred on any arbitrary substrate (i.e., denoted as transferred TiO_2 NM), including on SiO_2-coated (~80 nm) Si (100) substrates (Fig. 1c). The transferred NM was then heated at 60 °C to form stronger adhesion with substrates and the support layer was slowly detached (Fig. 1d).

Interestingly, the VO_2 sacrificial layer was dissolved selectively and rapidly in the dilute H_2O_2 solution with mild pH (~5.3) (Fig. 1b). The combination of the VO_2 sacrificial layer and H_2O_2 etchant for single-crystal rutile oxide NM in terms of release rate is as effective as that of a $Sr_3Al_2O_6$ sacrificial layer and H_2O for a single-crystal perovskite oxide NM[11]. The high etching capability of H_2O_2 on VO_2 was confirmed by direct comparison with that of an HNO_3 solution with the same concentration as a well-established VO_2 etchant with a strong acid (pH ~2)[24] (Supplementary Fig. 1): While the residue of VO_2 films remained even after 64 s after VO_2 films were immersed into strong acid HNO_3 solution, the H_2O_2 solution completely removed VO_2 films that were free of any residue on the surface of the TiO_2 substrate within 4 s. Furthermore, repeating H_2O_2 etching preserves the atomically flat surface topography, implying substrate reusability for the production of TiO_2 NM (Supplementary Fig. 2). VO_2 films

could be spontaneously oxidized by H_2O_2 and transformed to V_2O_5 and/or water-soluble $V_2O_5 \cdot nH_2O(s)$ gels with a layered van der Waals (vdW) structure along the c-axis[29,30]; these layered crystals with weak bonding are exfoliated and dispersed in the solution (Supplementary Fig. 3a, b). Since unreacted TiO_2 epitaxial layers cover whole surfaces of VO_2 sacrificial layers during the release process, the release of epitaxial TiO_2 NM by oxidation and dissolution of VO_2 sacrificial layers begins from the edge of the substrate (i.e., side etching); the dissolution (or release) time increases with the lateral size of the TiO_2 substrate (Supplementary Fig. 4).

As a result of effective dissolution of the VO_2 sacrificial layer by H_2O_2, the quality and alignment of epitaxial TiO_2 layers are intact during the release and transfer process as observed in symmetric 2θ-ω scans using synchrotron X-ray scattering (Fig. 2a). While the $(002)_R$ peak from the VO_2 sacrificial layer ($2\theta = 51.75°$) was clearly removed after the selective etching process (red line in Fig. 2a), the $(002)_R$ peak from ~ 40-nm-thick (001) TiO_2 single-crystal films with thickness oscillations was observed consistently at $2\theta = 49.54°$ in released (red line in Fig. 2a) and transferred TiO_2 NM on the Si substrate (blue line in Fig. 2a and Supplementary Fig. 5 with Cu $K_{\alpha1}$ X-ray radiation). Moreover, the $(002)_R$ peak from TiO_2 NM simultaneously appeared with a (400) peak from the Si substrate ($2\theta = 54.32°$) in the transferred TiO_2 NM (blue line in Fig. 2a), which represents that the c-axis of single-crystal TiO_2 NM was aligned with the out-of-plane orientation of the Si substrate. Azimuthal X-ray diffraction (XRD) ϕ scanning of $(112)_R$ crystallographic plane showed identical fourfold symmetry of released and transferred TiO_2 NMs with those of the single-crystal (001) TiO_2 host substrate (Supplementary Fig. 6); this result showed in-plane single-crystallinity of NMs without any rotated domains. Additionally, an electron backscatter diffraction (EBSD) map confirmed (001) orientation of rutile crystals over a large area in both as-grown and transferred TiO_2 layers (Fig. 2c).

To obtain more detailed information on the crystal structures of TiO_2 NMs during the release and transfer process, both in-plane and out-of-plane lattice parameters were monitored using reciprocal space mapping (RSM) around the (112) reflection of as-grown, released, and transferred 70-nm-thick TiO_2 layers (Fig. 2b). The RSM data clearly show sharp and intense (112) Bragg reflections and Kiessig fringes from the TiO_2 layer and substrates, and from the VO_2 sacrificial layers in as-grown heterostructures. Since 17-nm-thick VO_2 sacrificial layers are coherently grown on the TiO_2 substrates with identical H (i.e., in-plane reciprocal space unit), strain-free epitaxial TiO_2 layers with various thickness (10–70 nm) are coherently grown on VO_2/TiO_2 substrates (Fig. 2b and Supplementary Fig. 7b, c). After selective etching of the VO_2 sacrificial layer, H and L in released and transferred TiO_2 NM was identical with those in TiO_2 substrates and films in as-grown heterostructures; these strain-free TiO_2 layers with precisely controlled thickness are released and transferred onto a Si substrate without modification of the lattice parameters and crystallinity (Supplementary Fig. 7a).

Furthermore, surfaces of the released and transferred TiO_2 NM are uniform and intact without any defective boundaries[31]. Figure 2d shows that the entire area of TiO_2 films with lateral dimension of millimeter-scale and nanometer thickness was fully released from the VO_2/TiO_2 substrates after this etching process. Optical microscope (OM) images of transferred TiO_2 NM on the carbon TEM grid exhibit crack-free layers with natural wrinkles (Fig. 2e and Supplementary Fig. 8a). Both scanning electron microscope (SEM, Supplementary Fig. 8b) and atomic force microscope (AFM, Fig. 2f) images confirmed

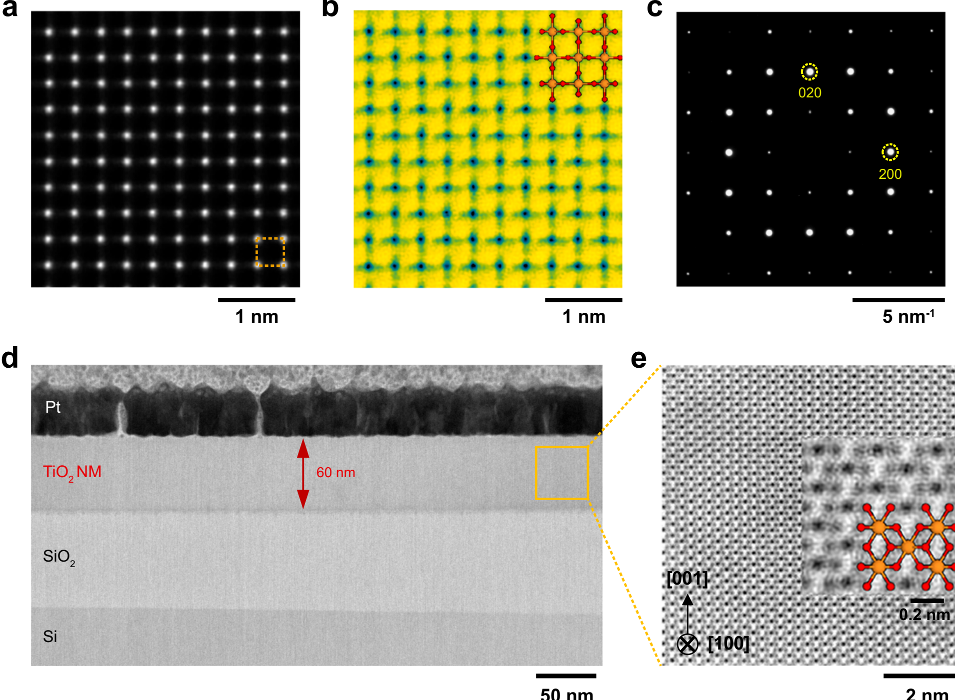

Fig. 3 STEM analysis of freestanding single-crystal TiO_2 nanomembrane (NM). **a** HAADF-STEM, **b** ABF-STEM, and **c** SADP images from the plane-view observation on 20-nm-thick freestanding TiO_2 NM. The white spots in HAADF-STEM, which are identical to Ti atoms, are consistent with cation sites of $[001]_R$-projected rutile structure. The atomic arrangement of ABF-STEM, visualization of oxygen atoms, was also identical to anion sites of rutile structure; the results indicate that atomic arrangement of freestanding TiO_2 NM was identical to the single-crystal rutile structure without defective features. **d**, **e** are the cross-sectional ABF-STEM images of TiO_2 NM, the quality of which is crystallographically high with perfect registry of Ti (orange color in **e**) and O (red color in **e**) atoms in rutile structure.

uniform and flat surface of both released and transferred TiO_2 NM without surface cracks or residues: the arithmetic average surface roughness of transferred TiO_2 NM ($R_a = 0.06$ nm) was comparable to that of originally grown TiO_2 films on VO_2/TiO_2 substrates ($R_a = 0.04$ nm), representing residue-free VO_2 removal by H_2O_2 etching and subsequent surface cleaning (Fig. 2f and Supplementary Figs. 9, 10).

High-resolution scanning transmission electron microscopy (STEM) confirms the local atomic structure of freestanding single-crystal TiO_2 NM. First, the released TiO_2 NM was transferred onto a TEM grid for STEM observation (Fig. 2e and Supplementary Fig. 11); the high-angle annular dark-field (HAADF) and the annular bright-field (ABF) STEM were applied for the plane-view observation. The HAADF-STEM image shows a square pattern of four titanium atoms (orange, dotted square) without a lattice distortion or defects (Fig. 3a). More interestingly, the ABF-STEM image shows the contrast tails from the titanium atom with contribution by the oxygen atoms and the pattern exactly matched the atomic structure of the rutile TiO_2 with the [001] zone axis (Fig. 3b). The selected-area diffraction pattern (SADP) provided that the in-plane lattice parameters of TiO_2 NM were 0.46 nm (Fig. 3c), which confirms the freestanding TiO_2 film was perfectly transferred. After the TiO_2 NM (~60 nm) was transferred to the SiO_2/Si substrate, cross-sectional STEM observation was performed with the [100] zone axis to visualize the structural coherency of the freestanding oxide NM, as shown in Fig. 3d, e. The low magnification ABF-STEM image shows that the TiO_2 NM is free of defects even after its transfer process from the wide field of view (Fig. 3d); the high magnification ABF-STEM image again verifies the perfect registry of Ti (orange) and oxygen (red) atoms in the rutile structure (Fig. 3e).

Heterogeneous integration of single-crystalline VO_2 films on the TiO_2-NM-templated Si substrates. After transfer to the (SiO_2-coated) Si substrates, the single-crystalline TiO_2 NMs served as templates for the epitaxial growth of high-quality VO_2 thin films on Si substrates (Fig. 1e). As observed in symmetric $2\theta - \omega$ scans, the intense $(002)_R$ VO_2 peak appeared at $\sim 2\theta = 51.85°$ along with peaks related to the TiO_2 template ($\sim 2\theta = 49.54°$) and Si substrates ($\sim 2\theta = 54.34°$) for the VO_2 films on the TiO_2-templated Si substrates (red line in Fig. 4a), compared to the absence of related peaks for the VO_2 films directly grown on Si substrate (black line in Fig. 4a); this result reveals that lattice-matched single-crystal templates facilitate the formation of epitaxial VO_2 films on Si substrates. Single-crystallinity of VO_2 films on TiO_2 NM/Si was again verified by identical fourfold symmetry with TiO_2 NM templates in asymmetric ϕ-scans of the $(112)_R$ plane (Fig. 4b). While the out-of-plane strain state of the TiO_2 NM did not change after the growth of VO_2 films, the out-of-plane lattice parameters of VO_2 films (2.838 Å) were reduced compared to those of bulk VO_2 (2.88 Å). Indeed, an RSM near the (112) reflection of the TiO_2 NM confirms that the peaks from the VO_2 films and TiO_2 NM showed identical H (i.e., in-plane reciprocal space unit) (Fig. 4c), which indicates that a 10-nm-thick VO_2 film remains coherently strained to the TiO_2 NM along the in-plane direction[27,28].

Low magnification ABF- and high magnification HAADF-STEM images (Fig. 4d, e) confirm that the epitaxial growth of 10-nm-thick VO_2 on TiO_2 NM can realize heterogeneous integration of single-crystal VO_2 films on a Si substrate. In particular, VO_2 and TiO_2 are coherently matched and the interface can be visualized due to the slight contrast difference between VO_2 and TiO_2, as indicated by the arrow (Fig. 4e); the atomic resolution image implicates that the VO_2 layer is tightly constrained from the underlying TiO_2 NM, and thus

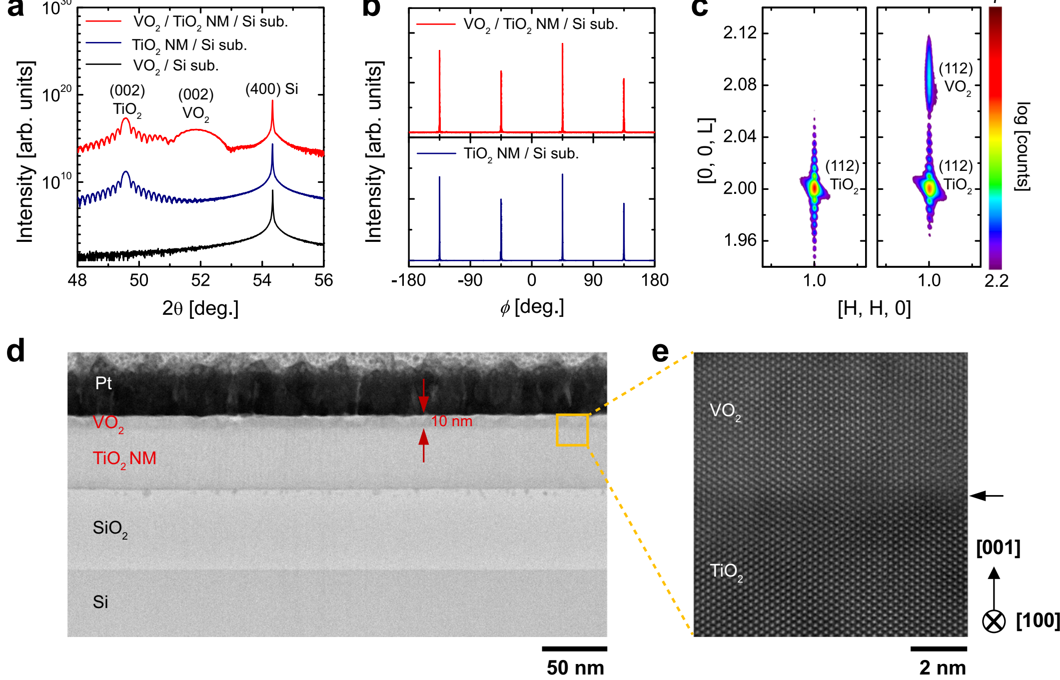

Fig. 4 Heterogeneous integration of rutile oxide epitaxial VO_2/TiO_2 heterostructures on Si substrates. a Symmetric $2\theta - \omega$ scan, **b** asymmetric ϕ scan, and **c** reciprocal space mapping around (112) reflection of TiO_2 NM on Si substrates before (blue in **a**, **b**, and left in **c**) and after (red in **a**, **b**, and right in **c**) the growth of VO_2 films, implying single-crystallinity of coherently strained VO_2 films on TiO_2 NM/Si. **d** The cross-sectional ABF-STEM images of the heterogeneous VO_2/TiO_2 NM on SiO_2/Si. The atomic-scale HAADF-STEM image at the area indicated by the yellow square in **d** is shown in **e** (zone axis: [100] in TiO_2).

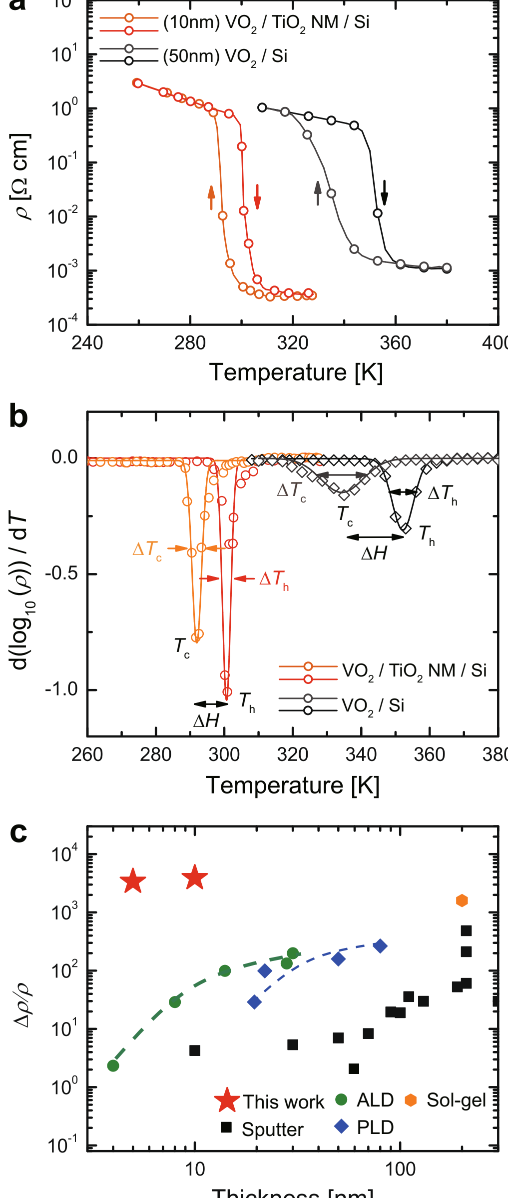

Fig. 5 Single-crystalline VO_2 films with steep phase transition on TiO_2-NM-templated Si substrate. a Temperature-dependent resistivity modulation near T_{MIT} in 10-nm-thick VO_2 films on TiO_2 NM/SiO_2/Si (red lines) and 50-nm-thick VO_2 films on SiO_2/Si (black lines). **b** Comparison of various metal-insulator transition properties ($d(\log_{10}(\rho))/dT$, T_h, T_c, ΔH, ΔT_h, ΔT_c) between 10-nm-thick VO_2 films on TiO_2 NM/SiO_2/Si (red lines) and 50-nm-thick VO_2 films on SiO_2/Si (black lines). Note that the transition width and sharpness, as well as the resistivity ratio, were substantially improved in VO_2 films with TiO_2 NM, compared to those without TiO_2 NM. **c** Benchmark of resistivity ratio $\Delta\rho/\rho = (\rho_{T_{MIT}-15K} - \rho_{T_{MIT}+15K})/\rho_{T_{MIT}+15K}$ for VO_2 films on Si substrates across the MIT. For a direct comparison, all films were grown on oxide-coated Si substrates using various growth techniques: (sputtering (black square), ALD (green circle), PLD (blue diamond), and sol-gel (orange hexagon)) reported in the previous literature (Supplementary Table 1). While deteriorated $\Delta\rho/\rho$ was observed in VO_2 films directly grown on Si due to the polycrystallinity of the films and the formation of a defective interfacial layer, epitaxial growth of VO_2 films (5 and 10 nm) guided by transferred TiO_2 NM enables integration of correlated oxides on silicon substrates with the highest modulation of resistivity ratio across the metal-insulator transition (red stars).

TiO_2 NM templates between VO_2 and Si enable the growth of epitaxial VO_2 films with crystallographic perfection free from defects.

To benchmark the quality of the VO_2 thin films on the TiO_2-NM-templated SiO_2/Si substrates in terms of MIT, temperature-dependent resistivity was measured for VO_2 films depending on the existence of transferred TiO_2 NM. Higher resistivity modulation ($\Delta\rho/\rho \sim 3.3\times10^3$) was observed across $T_{MI} \sim 296$ K in both 5-nm-thick and 10-nm-thick VO_2 on TiO_2 NM/SiO_2/Si (red line in Fig. 5a and Supplementary Fig. 13b) than in 10-nm-thick VO_2 on SiO_2/Si (Supplementary Fig. 13a) and even in 50-nm-thick VO_2 on SiO_2/Si ($\Delta\rho/\rho \sim 5.2\times10^2$ across the $T_{MI} \sim$ 343 K) (black line in Fig. 5a). In addition to the resistivity ratio, other MIT properties ($d(\log_{10}(\rho))/dT$, T_h, T_c, ΔH, ΔT_h, ΔT_c) were characterized as shown in Fig. 5b[32]. $d(\log_{10}(\rho))/dT$ was plotted and fitted with a Gaussian function. T_h and T_c were then defined at the peak position of the Gaussian and the transition width was calculated from the difference ($\Delta H = T_h - T_c$). The transition sharpness ΔT_h and ΔT_c was estimated from the full-width at half-maximum of the Gaussian peak. In fact, the transition width and sharpness, as well as the resistivity ratio, were significantly improved in the VO_2 films with TiO_2 NM (i.e., 8.70 and 3.3 K for ΔH and ΔT_c, respectively) compared to those without TiO_2 NM (i.e., 17.94 and 14.54 K for ΔH and ΔT_c, respectively). The sharpened phase transition is attributed to the single-crystalline nature of the VO_2 films perfectly aligned with the underlying single-crystal TiO_2 NM templates. Moreover, the transferred single-crystal TiO_2 NM forms coherently tensile-strained VO_2 films; this epitaxial strain leads to a T_{MI} shift close to room temperature in VO_2 films on TiO_2 NM/SiO_2/Si compared to relaxed VO_2 films on SiO_2/Si substrates[27,28,32]. Along with steep MIT under temperature, these single-crystalline VO_2 films on TiO_2 NM/Si show high endurance during thermal and electrical cycling. Both thermally induced MIT and electrically induced MIT ($I_{on}/I_{off} > 10^3$) were consistently observed without any drift during the multiple cycles of thermal switching (Supplementary Fig. 14) and electrical switching (Supplementary Fig. 15), respectively.

Discussion

It should be noted that the integration of VO_2 films with excellent electrical properties on a Si substrate has proved challenging due to fundamental limitations. A representative set of data of MIT properties from VO_2 thin films on Si (or oxide-coated Si or buffered Si) substrates was compiled to allow for a direct comparison with those from our films (Fig. 5c, Supplementary Table 1, and Supplementary Fig. 16). Despite previous attempts to directly grow VO_2 thin films on Si substrates using various deposition techniques, $\Delta\rho/\rho$ across the T_{MI} deteriorated due to the formation of polycrystallinity of the films. Notably, a further reduction in $\Delta\rho/\rho$ was found to occur with decreasing film thickness, likely due to the formation of defective interfacial layers (e.g., by thermodynamic reaction of VO_2 with Si (or SiO_2)); the cation-to-anion stoichiometry was not maintained in the VO_2 films near the interface[33,34]. If this compositional variation (i.e., off-stoichiometry) contains a significant fraction of the films, the resistivity ratio and transition sharpness will significantly degrade in the regime of an ultrathin thickness (<40 nm), as observed in our 10-nm-thick VO_2 films on SiO_2/Si and Al_2O_3-buffered Si (Supplementary Figs. 13, 16); steeper transition cannot be engineered simply by direct deposition of thin VO_2 films on Si substrates due to the existence of interfacial layers and the substantial density of defects.

However, the TiO_2 template NM on Si substrates permits epitaxy with VO_2 thin films due to its identical crystal structure ($P4_2/mnm$) and small lattice mismatch (f_a ~ 0.86%). The transferred NM could play a crucial role as a seed layer for epitaxy, and artificially allows the first demonstration on heterogeneous integration of single-crystalline VO_2 on Si substrates, which are commonly employed in electronic devices. Furthermore, the TiO_2 NM is likely to prevent subsequent reaction between VO_2 and the Si substrate, and allows excellent control over the V-oxidation states without any extended defects[33,34]. Thus, epitaxial growth of ultrathin VO_2 films guided by transferred TiO_2 NM enables integration of correlated oxides with unprecedented modulation of the resistivity ratio ($\triangle\rho/\rho > 10^3$) across the MIT in the regime of an ultrathin thickness (5–10 nm) on Si substrates (see red stars in Fig. 5c).

In summary, heterogeneous integration of a freestanding single-crystalline rutile oxide NM was achieved by exploiting selective oxidation and dissolution of isostructural sacrificial layers. Despite a mild pH condition under a dilute H_2O_2 solution at room temperature, VO_2 sacrificial films are spontaneously oxidized by H_2O_2 and transformed to layered crystals, which in turn could be exfoliated and dispersed in solution to release and transfer the millimeter-scale TiO_2 NM with controlled thickness on oxide-coated Si substrates. Owing to the nearly perfect single-crystallinity of the transferred rutile TiO_2 NM, this lattice-matched single-crystal template permits heterogeneous integration of epitaxial VO_2 films on Si substrates; exceptional MIT characteristics in terms of transition sharpness ($\triangle T_h$ ~ 2.85 K and $\triangle T_c$ ~ 3.3 K) and resistivity ratio ($\triangle\rho/\rho > 10^3$) were realized in ultrathin VO_2 films integrated on Si substrates, benefitting from the superior quality of epitaxial oxide films.

Our strategy to release and transfer a freestanding epitaxial rutile oxide NM for a MIT will provide an unprecedented platform using emergent phenomena in epitaxial oxide heterostructures to be integrated with current state-of-the-art Si-based technology (e.g., integrated electronics[3,6] and photonics[13,35] on Si). For example, our epitaxial oxide NM with steep phase transition could deliver a hybrid optical modulator with a high extinction ratio, low loss, and high modulation speed integrated on Si waveguides[13,35,36]. Moreover, our approach for single-crystalline oxide NMs with high thermal stability are generally applicable for heterogeneous integration of high-quality oxide NM with any rutile crystal structures on Si substrates (e.g., epitaxial growth of metallic RuO_2 single-crystalline NMs on transferred TiO_2 NM/Si or direct transfer of metallic RuO_2 single-crystal NMs on Si, Supplementary Figs. 17–20); our study enables us to extend the materials spectrum for freestanding single-crystalline rutile oxide NM by developing a new combination of sacrificial layer and etchant. It also offers a unique opportunity for new types of artificial heterostructures by stacking multi-functional oxide NMs with other 2D/3D single-crystalline NMs (e.g., III–V, exfoliated 2D layered materials, complex oxides)[10,17] or by controlling twisted angle between two misaligned sheets of oxide NMs (similar to twisted bilayer graphene heterostructure with atomic and electronic reconstruction)[37,38] for novel interfacial physics and a new generation of emergent devices.

Methods

Epitaxial film growth. The epitaxial VO_2 thin films (~17 nm) were grown on (001) TiO_2 single-crystal substrates, followed by the growth of TiO_2 films (10–70 nm) by PLD. First, (001) TiO_2 single-crystal substrates (Shinkosha CO., LTD) with lateral size of up to 5 mm × 5 mm were loaded into the PLD chamber, which was then evacuated to a base pressure of ~1×10^{-6} Torr. The rotating V_2O_5 and TiO_2 targets were then ablated by focusing a KrF excimer laser (Coherent Complex Pro 102 F, $\lambda = 248$ nm) with a fluence of 1 J/cm^2 and a repetition rate of 1 Hz. The growth of VO_2 films was performed at fixed $P_{O_2} = 15$ mTorr and $T_g = 300$ °C, which were selected to induce a steep MIT near room temperature from coherently tensile-strained VO_2 films. Subsequently, TiO_2 films were grown on VO_2 templates under $P_{O_2} = 28$ mTorr and $T_g = 300$ °C. After the growth of heterostructure, the samples were cooled to room temperature at a rate of 20 °C/min. The epitaxial VO_2 film (5–10 nm) was grown on the transferred TiO_2 NM/Si with an identical growth condition of that of VO_2 sacrificial layers on the (001) TiO_2 substrate.

Release and transfer of freestanding TiO_2 NMs. To release the freestanding TiO_2 NM from the VO_2/TiO_2 substrates, the surface of the grown heterostructure was adhered onto a rigid supporting layer (e.g., polydimethylsiloxane, thermal release tape (Haeun Chemtec, RP70N5)). The structure was immersed in a dilute H_2O_2 solution until the sacrificial VO_2 layer was completely dissolved. To transfer the released TiO_2 NM to other substrates, TiO_2 NM was placed onto an oxide-coated silicon substrate and exposed to an appropriate temperature. Finally, the freestanding NM remained on the silicon substrate after peeling off the rigid supporting layer slowly. The structure was immersed in a dilute 10% H_2O_2 solution (i.e., 50 ml of 35% H_2O_2 + 150 ml of H_2O) at room temperature until the sacrificial VO_2 layer was completely dissolved, with the freestanding NM left on the rigid supporting layer. After dissolving the VO_2 layers in H_2O_2, H_2O residue on the released TiO_2 surface was evaporated in a vacuum desiccator for 10 min. To transfer the released TiO_2 NM to other substrates (such as thermally grown SiO_2-coated silicon), the TiO_2 NM/rigid supporting layer was attached to a oxide-coated silicon substrate and was heated to 60–80 °C for 10 min. Finally, the freestanding NM remained on the silicon substrate after peeling off the rigid supporting layer slowly.

SEM, EBSD, and AFM measurements. OM images were recorded using BX53M (Olympus, Tokyo, Japan) microscope, equipped with an objective MPlanFL N (Olympus) and i-solution IMT cam CCD camera. The SEM and EBSD measurements were made using an XL30SFEG and FEI Helios Nanolab 650 equipped with an EBSD detector, respectively. The EBSD pattern was acquired by an EDAX Hikari EBSD camera while the sample was tilted at 70° and scanned with an electron beam of 25 nA at 20 kV. The measured data were analyzed using TSL OIM Analysis7. The AFM images were obtained using a VEECO Dimension 3100 in tapping mode.

X-ray diffraction (XRD) and X-ray absorption spectroscopy (XAS). High-resolution x-ray scattering was performed by using synchrotron radiation at the 3D XRS (λ ~ 0.12398 nm, energy ~10 keV at Si (111)) beamline of Pohang Light Source-II (PLS-II, Pohang, Republic of Korea), and using an in-house HRXRD (Bruker Discover 8 X-ray diffractometer) with Cu $K_{\alpha 1}$ radiation (λ ~ 0.15406 nm). The detailed information on in-plane and out-of-plane lattice parameters and strain states of each films and NM was obtained by using both symmetric 2θ-ω scan and asymmetric RSM around the (112) reflection. X-ray absorption spectroscopy (XAS) was performed using the 2 A MS beamline at PLS-II. The total electron yield mode with an energy resolution of ~0.1 eV was used for measurement at a base pressure of 5×10^{-10} Torr in the analysis chamber by measuring the sample current (I_1) divided by the beam current (I_0) to remove the variation of the beam intensity.

Scanning transmission electron microscope (STEM). Two sample types were prepared for plane-view STEM imaging of transferred TiO_2 NM on a carbon TEM grid and cross-sectional STEM imaging of transferred TiO_2 NM and VO_2/TiO_2 hetero-NM on SiO_2/Si. For the plane-view observation, the TiO_2 film was directly transferred onto the carbon TEM grid; $TiO_2/VO_2/TiO_2$ epitaxial heterostructure was physically attached to the PDMS with the carbon TEM grid and immersed in a dilute H_2O_2 solution. After selective oxidation and dissolution of the VO_2 sacrificial layer, the single-crystal TiO_2 NM was naturally released and attached to the carbon TEM grid (Supplementary Fig. 4). For the cross-sectional observation, the transferred TiO_2 NM and VO_2/TiO_2 hetero-NM on SiO_2/Si substrates were prepared by a focused ion beam (FIB) system (Helios G3, FEI), in which the samples were thinned by a Ga ion beam. The atomic structures were observed using a STEM (JEOL ARM 200 F, JEOL Ltd., Japan) with a fifth-order aberration corrector (ASCOR, CEOS GmbH, Heidelberg, Germany); the probe diameter and convergence angle of the beam were ~0.7 Å and ~27 mrad under an acceleration voltage of 200 kV, respectively. The collection semi-angles of the detectors for HAADF imaging were 54–210 mrad, and those for ABF imaging were 8–16 mrad to detect light elements (i.e., oxygen). The obtained STEM images were local difference filtered to reduce background noise (HREM Research Inc., Japan).

Resistivity measurements. The resistivity (ρ) was measured in the van der Pauw geometry during heating and cooling from 260 to 380 K by using a chamber probe station equipped with a Hall measurement system and a temperature control system. The resistivity change over the MIT ($\Delta\rho/\rho$) was defined as $\Delta\rho/\rho = (\rho_{T_{MIT}-15K} - \rho_{T_{MIT}+15K})/\rho_{T_{MIT}+15K}$. The fitting of the derivative of $\log_{10}(\rho)$ as a function of temperature (K) was performed based on the Gaussian function. T_h and T_c were then defined at the peak position of the Gaussian and the transition width was calculated from the difference ($\triangle H = T_h - T_c$). The transition sharpness $\triangle T_h$ and $\triangle T_c$ was estimated from the full-width at half-maximum of the Gaussian peak.

Data availability

All relevant data within the article are available from the corresponding authors on reasonable request.

Received: 24 November 2020; Accepted: 29 June 2021;
Published online: 18 August 2021

References

1. Kroemer, H. Nobel lecture: quasielectric fields and band offsets: teaching electrons new tricks. *Rev. Mod. Phys.* **73**, 783–793 (2001).
2. Akasaki, I. Nobel lecture: fascinated journeys into blue light. *Rev. Mod. Phys.* **87**, 1119–1131 (2015).
3. Zhou, Y. & Ramanathan, S. Mott memory and neuromorphic devices. *Proc. IEEE* **103**, 1289–1310 (2015).
4. Yang, Z., Ko, C. & Ramanathan, S. Oxide electronics utilizing ultrafast metal-insulator transitions. *Annu. Rev. Mater. Res.* **41**, 337–367 (2011).
5. Lee, D. et al. Isostructural metal-insulator transition in VO_2. *Science* **362**, 1037–1040 (2018).
6. del Valle, J. et al. Subthreshold firing in Mott nanodevices. *Nature* **569**, 388–392 (2019).
7. Ohtomo, A. & Hwang, H. Y. A high-mobility electron gas at the $LaAlO_3$/$SrTiO_3$ heterointerface. *Nature* **427**, 423–426 (2004).
8. Khan, A. I. et al. Negative capacitance in a ferroelectric capacitor. *Nat. Mater.* **14**, 182–186 (2015).
9. Kum, H. et al. Epitaxial growth and layer-transfer techniques for heterogeneous integration of materials for electronic and photonic devices. *Nat. Electron* **2**, 439–450 (2019).
10. Kum, H. S. et al. Heterogeneous integration of single-crystalline complex-oxide membranes. *Nature* **578**, 75–81 (2020).
11. Lu, D. et al. Synthesis of freestanding single-crystal perovskite films and heterostructures by etching of sacrificial water-soluble layers. *Nat. Mater.* **15**, 1255–1260 (2016).
12. Lu, D., Crossley, S., Xu, R. J., Hikita, Y. & Hwang, H. Y. Freestanding oxide ferroelectric tunnel junction memories transferred onto silicon. *Nano Lett.* **19**, 3999–4003 (2019).
13. Briggs, R. M., Pryce, I. M. & Atwater, H. A. Compact silicon photonic waveguide modulator based on the vanadium dioxide metal-insulator phase transition. *Opt. Express* **18**, 11192–11201 (2010).
14. Matthews, J. W. & Blakeslee, A. E. Defects in epitaxial multilayers:I. Misfit dislocations. *J. Cryst. Growth* **27**, 118–125 (1974).
15. Pellegrino, L. et al. Multistate memory devices bbased on free-standing VO_2/TiO_2 microstructures driven by joule self-heating. *Adv. Mater.* **24**, 2929–2934 (2012).
16. Sim, J. S., Zhou, Y. & Ramanathan, S. Suspended sub-50 nm vanadium dioxide membrane transistors: fabrication and ionic liquid gating studies. *Nanoscale* **4**, 7056–7062 (2012).
17. Rogers, J. A., Lagally, M. G. & Nuzzo, R. G. Synthesis, assembly and applications of semiconductor nanomembranes. *Nature* **477**, 45–53 (2011).
18. Roberts, M. M. et al. Elastically relaxed free-standing strained-silicon nanomembranes. *Nat. Mater.* **5**, 388–393 (2006).
19. Yablonovitch, E., Gmitter, T., Harbison, J. P. & Bhat, R. Extreme selectivity in the lift-off of epitaxial GaAs films. *Appl. Phys. Lett.* **51**, 2222–2224 (1987).
20. Wong, W. S., Sands, T. & Cheung, N. W. Damage-free separation of GaN thin films from sapphire substrates. *Appl. Phys. Lett.* **72**, 599–601 (1998).
21. Jang, H. W. et al. Strain-induced polarization rotation in epitaxial (001) $BiFeO_3$ thin films. *Phys. Rev. Lett.* **101**, 107602 (2008).
22. Geim, A. K. & Grigorieva, I. V. Van der Waals heterostructures. *Nature* **499**, 419–425 (2013).
23. Yamin, T., Wissberg, S., Cohen, H., Cohen-Taguri, G. & Sharoni, A. Ultrathin films of VO_2 on r-cut sapphire achieved by postdeposition etching. *ACS Appl. Mater. Interfaces* **8**, 14863–14870 (2016).
24. Wang, N., Peh, Y. K., Magdassi, S. & Long, Y. Surface engineering on continuous VO_2 thin films to improve thermochromic properties: top-down acid etching and bottom-up self-patterning. *J. Colloid Inter. Sci.* **512**, 529–535 (2018).
25. Hong, S. S. et al. Extreme tensile strain states in $La_{0.7}Ca_{0.3}MnO_3$ membranes. *Science* **368**, 71–76 (2020).
26. Paskiewicz, D. M., Sichel-Tissot, R., Karapetrova, E., Stan, L. & Fong, D. D. Single-crystalline $SrRuO_3$ nanomembranes: a platform for flexible oxide electronics. *Nano Lett.* **16**, 534–542 (2016).
27. Park, Y. et al. Directional ionic transport across the oxide interface enables low-temperature epitaxy of rutile TiO_2. *Nat. Commun.* **11**, 1401 (2020).
28. Muraoka, Y. & Hiroi, Z. Metal-insulator transition of VO_2 thin films grown on TiO_2 (001) and (110) substrates. *Appl. Phys. Lett.* **80**, 583–585 (2002).
29. Livage, J. Vanadium pentoxide gels. *Chem. Mater.* **3**, 578–593 (1991).
30. Fang, G. D. et al. A mechanistic understanding of hydrogen peroxide decomposition by vanadium minerals for diethyl phthalate degradation. *Environ. Sci. Technol.* **52**, 2178–2185 (2018).
31. Guo, Y. W. et al. A reconfigurable remotely epitaxial VO_2 electrical heterostructure. *Nano Lett.* **20**, 33–42 (2020).
32. Zhang, H. T. et al. Wafer-scale growth of VO_2 thin films using a combinatorial approach. *Nat. Commun.* **6**, 8475 (2015).
33. Peter, A. P. et al. Metal-insulator transition in ALD VO_2 ultrathin films and nanoparticles: morphological control. *Adv. Funct. Mater.* **25**, 679–686 (2015).
34. Yang, Z. & Ramanathan, S. Direct measurement of compositional complexity-induced electronic inhomogeneity in VO_2 thin films grown on gate dielectrics. *Appl. Phys. Lett.* **98**, 192113 (2011).
35. Joushaghani, A. et al. Wavelength-size hybrid Si-VO_2 waveguide electroabsorption optical switches and photodetectors. *Opt. Express* **23**, 3657–3668 (2015).
36. Lee, D. et al. Sharpened VO_2 phase transition via controlled release of epitaxial strain. *Nano Lett.* **17**, 5614–5619 (2017).
37. Cao, Y. et al. Unconventional superconductivity in magic-angle graphene superlattices. *Nature* **556**, 43 (2018).
38. Yoo, H. et al. Atomic and electronic reconstruction at the van der Waals interface in twisted bilayer graphene. *Nat. Mater.* **18**, 448–453 (2019).

Acknowledgements

We acknowledge support for this work by the Basic Science Research Program (2020R1A4A1018935 and 2020R1A2C2006389) through the National Research Foundation of Korea (NRF) funded by the Ministry of Science and ICT and the Korea Basic Science Institute (National Research Facilities and Equipment Center) Grant funded by the Ministry of Education (2020R1A6C101A202). D.K.L., Y.P., and J.S. acknowledge the support by the Samsung Research Funding & Incubation Center of Samsung Electronics under Project Number SRFC-TA1703-09. Y.P. acknowledges the support by the Basic Science Research Program through the National Research Foundation of Korea (NRF) funded by the Ministry of Education (2020R1A6A3A13075514). This study was partially supported by Brain Korea 21 Four for education and research center for future materials (F21YY7105002).

Author contributions

J.S., D.K.L., and Y.P. conceived the idea and designed the study with assistance from C.-B.E.; D.K.L. and Y.P. developed the fabrication process of freestanding nanomembranes, performed the growth of heterostructures, XRD, XAS, SEM, EBSD, AFM, and electrical transport measurement with assistance from J.P. and Y.K.; H.S., G.-Y.K., and S.-Y.C. characterized the nanomembranes by STEM; Y.K. assisted synchrotron spectroscopy measurement; J.S., D.K.L., Y.P., S.-Y.C., and H.S. wrote the manuscript and all authors commented on it; J.S. directed the overall research.

Competing interests

The authors declare the following competing financial interest(s): D.K.L., Y.P., H.S., S.-Y.C., and J.S. are co-inventors on a patent application based on the results of this work filed by Pohang University of Science and Technology.

Additional information

Supplementary information The online version contains supplementary material available at https://doi.org/10.1038/s41467-021-24740-2.

Correspondence and requests for materials should be addressed to S.-Y.C. or J.S.

Peer review information *Nature Communications* thanks Jian Shi and other, anonymous, reviewers for their contributions to the peer review of this work. Peer review reports are available.

Reprints and permission information is available at http://www.nature.com/reprints

Publisher's note Springer Nature remains neutral with regard to jurisdictional claims in published maps and institutional affiliations.

Open Access This article is licensed under a Creative Commons Attribution 4.0 International License, which permits use, sharing, adaptation, distribution and reproduction in any medium or format, as long as you give appropriate credit to the original author(s) and the source, provide a link to the Creative Commons license, and indicate if changes were made. The images or other third party material in this article are included in the article's Creative Commons license, unless indicated otherwise in a credit line to the material. If material is not included in the article's Creative Commons license and your intended use is not permitted by statutory regulation or exceeds the permitted use, you will need to obtain permission directly from the copyright holder. To view a copy of this license, visit http://creativecommons.org/licenses/by/4.0/.

© The Author(s) 2021